Universiteit Utrecht

SRON
Netherlands Institute for Space Research

Bachelor Thesis

Investigation of the high-energy temporal characteristics of magnetar 4U 0142+61 covering a 16 year period

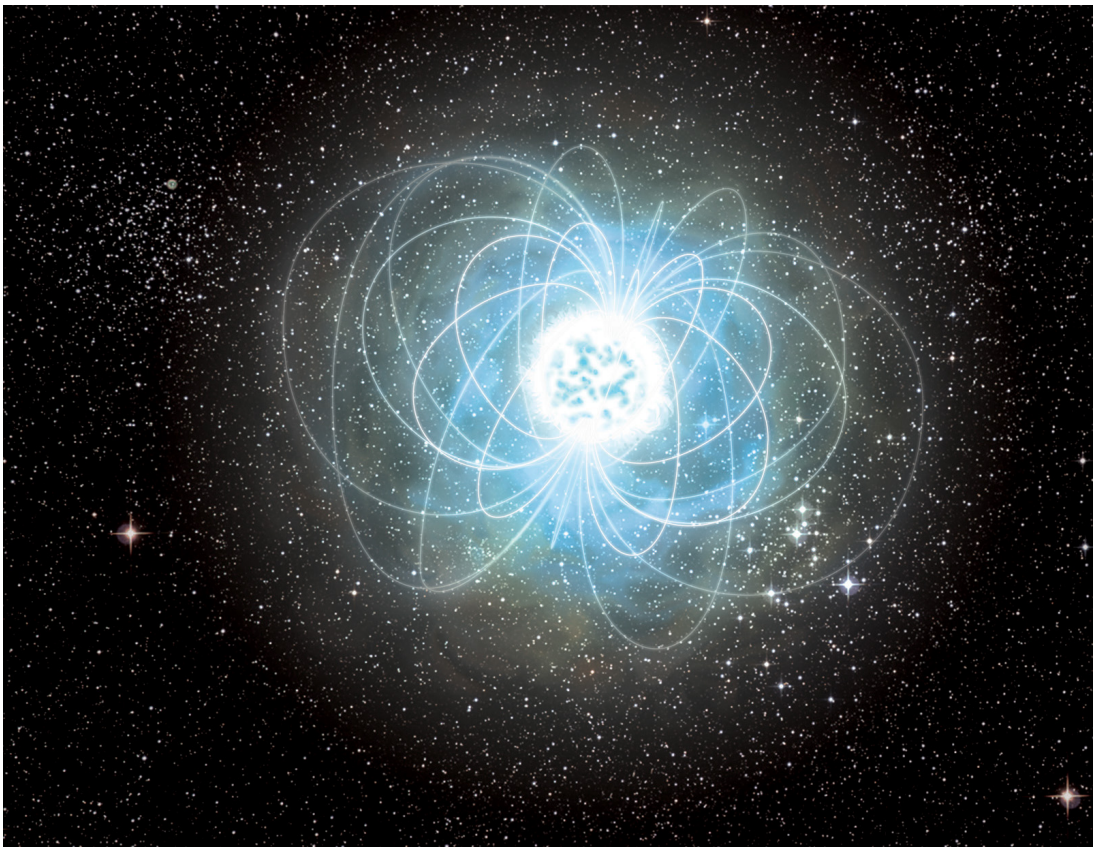

Author:
Matthijs van Groeningen
Study:
Physics & Astronomy
Utrecht University

Supervisor:
Dr. Lucien Kuiper
SRON
Utrecht University contact:
Dr. Tomislav Prokopec
Utrecht University

June 19, 2019

Abstract

In this bachelor project the temporal characteristics of magnetar 4U 0142+61 have been investigated using *unexplored* INTEGRAL ISGRI soft gamma-ray data in the 20-300 keV band, collected since Aug. 15, 2010 up to Jan. 21, 2019, and Fermi-LAT high-energy gamma-ray data (>30 MeV), collected since Aug. 4, 2008 up to Jan. 21, 2019.
Essential in this study is the availability of pulsar ephemerides i.e. timing models describing the rotation behaviour of the pulsar very accurately as a function of time for a certain time interval. Data from concurrent monitoring observations (commenced on July 29, 2011 and ceased at March 26, 2019) of 4U 0142+61 performed by the Swift-XRT instrument (0.3-10 keV) have been used to construct these required timing models.
In this work I prepared an accurate timing model for the period July 29, 2011 – Feb. 26, 2015, covering more then 3.5 years, after downloading and pipeline reprocessing Swift-XRT data taken in Windowed-Timing (WT) mode. This model was subsequently applied and verified using hard X-ray data (3-79 keV) from observations taken by the NuSTAR telescope during March 27–29, 2014. Comparison with the contemporaneous Swift-XRT data yielded a consistent picture in the overlapping energy interval i.e. 3-10 keV, while the full picture clearly showed the well-known morphology changes of the pulse profile as function of energy, but now in (much) more detail.
Using the full set of Swift-XRT based ephemerides the *unexplored* soft gamma-ray data from the coded mask ISGRI instrument (20-300 keV) aboard INTEGRAL were processed in a timing analysis - after observation selection and data screening - to yield pulse-phase distributions across the 20-300 keV band. From these distributions (integrated across Aug. 15, 2010 up to Jan. 21, 2019) the significances of the pulsed emission have been estimated (and the morphology changes versus energy revealed) for various energy bands between 20 and 300 keV. I obtained signal strengths of $4.2\sigma, 4.3\sigma, 3.4\sigma$ and 1.3σ for the 20-50, 50-100, 100-150 and 150-300 keV bands, respectively, while the integral band, 20-150 keV, yielded a 6.9σ signal.
Combining these new ISGRI results with existing ISGRI products from the 2003-2010 period yielded the most accurate pulse profiles currently available, covering the full ~ 16 year INTEGRAL data period from 2003 to 2019. The overall pulsed emission significances are $6.7\sigma, 6.2\sigma, 5.4\sigma$ and 1.3σ for the 20-50, 50-100, 100-150 and 150-300 keV bands, respectively. The overall 20-150 keV signal reached even a 10.7σ strength.
Furthermore, the full set of Swift-XRT based ephemerides, along with some archival RXTE-PCA based ephemerides for the 2008–2011 period, has been used in a timing analysis of Fermi-LAT (>30 MeV) high-energy gamma-ray data in order to investigate the presence of pulsed emission at high-energy gamma-rays. I found *no* evidence for pulsed emission of 4U 0142+61 above >30 MeV in any energy band using more than 10 years of Fermi-LAT observations.
From the newly derived mission-wide INTEGRAL ISGRI (16 years) and Fermi-LAT (10 years) pulse-phase distributions spectral information of the pulsed emission can be reconstructed to yield the pulsed spectrum in great detail across the 20 keV - 10 GeV range, however, this is outside the scope of this bachelor project.

Title page image: artist impression of a magnetar by Lucy Conklin [1].

Contents

Chapter 1

Introduction

In space, there are many interesting and exotic objects to be found. One of these objects is a so-called magnetar. Magnetars constitute a special class of neutron stars. Like other neutron stars, they are relatively small, very dense objects, consisting mainly of tightly packed neutrons and they emerge from the violent deaths of massive stars. In particular, magnetars are characterized by their extremely strong magnetic fields.
A fundamental piece of information in our understanding of magnetars is the characterization of their pulsed high-energy spectrum, i.e. to what degree they emit X-rays and gamma-rays. An accurate description of the pulsed high-energy spectrum will be of great benefit for testing theories regarding the structure and geometry of the magnetosphere of magnetars. To examine the pulsed high-energy spectrum of a magnetar we first need an accurate description of its high-energy temporal characteristics. These characteristics can be obtained after applying accurate timing models (ephemerides) in a pulse-phase folding process to obtain pulse-phase distributions for different energy bands. The research presented in this bachelor thesis aims to investigate these high-energy temporal characteristics and thereby serves mainly as preparatory work for investigating the pulsed high-energy spectrum.
In this bachelor thesis I have focused on one magnetar, dubbed 4U 0142+61. Several space telescopes have observed 4U 0142+61 over the last decades since its discovery by the Uhuru satellite in 1978 [2]. These observations have led to a substantial amount of data of which the largest part had already been thoroughly analyzed before this research. However, the data from the last decade had been left relatively untouched. In particular, data from INTEGRAL's ISGRI instrument (sensitive to hard X-rays/soft gamma-rays between 20 and 300 keV) of 4U 0142+61 collected between Aug. 15, 2010 and Jan 21, 2019 had yet to be analyzed. This has been done in this research. By adding the observations from this period to the existing set (2003 - 2010), I have studied approximately twice the amount of INTEGRAL ISGRI data compared to previous research [3].
In addition to the INTEGRAL ISGRI data, I have also analyzed the observations of the Large Area Telescope (LAT) aboard gamma-ray telescope Fermi, which was launched June 11, 2008. The LAT is sensitive to gamma-rays >30 MeV and thus a suitable instrument for studying potential high-energy gamma-ray radiation of 4U 0142+61. Previous research that used the Fermi-LAT instrument to study 4U 0142+61 did not find significant evidence of radiation with energy >30 MeV [4][5][6]. The most recent study [6] used approximately 6 years (Aug. 4, 2008 – Oct. 1, 2014) of Fermi-LAT data. For this research more than 10 years (Aug. 4 2008 – Jan. 21, 2019) of Fermi-LAT data have been used.

Chapter 2

Theoretical aspects

2.1 Stellar evolution

Stars are giant spheres of hot gas that consist mostly of hydrogen contained by self-gravitation. They fuel themselves by means of nuclear fusion of hydrogen into helium in the core of the star. This produces a force that counteracts the gravitational pull on the outer layers and prevents the star from collapsing under its own gravity. This equilibrium sustains the star for most of its lifetime.
When its hydrogen reserves in the core are depleted, it marks the beginning of a transition to what we call a stellar remnant. As the gravitational pressure on the core start to outweigh the core's nuclear pressure, the core starts to contract. In this process gravitational energy gets converted to thermal energy. This raises the core's temperature which heats the layer just outside the core, allowing the hydrogen there to fuse. This hydrogen fusing shell eats its way outward, leaving behind a growing helium core. The core eventually becomes so massive that its electrons become degenerate, meaning that the Pauli exclusion principle prevents them from getting any closer together. What follows depends on the mass of the star, however a common feature is the blowing away of the outer layers of the star and leaving behind a compact object.

2.1.1 Evolution of low-mass stars

For stars with a mass high enough for fusion to occur but smaller than approximately $5M_\odot$, the core becomes so hot that helium starts to fuse into carbon (and a little bit of oxygen). An onion-like shell structure is produced, with the core containing mostly carbon, the first shell fusing helium into carbon and a second shell fusing hydrogen into helium. This structure eventually causes the star to blow away its outer layers, leaving behind a dense core sustained by electron degeneracy against gravitational collapse. The stellar remnant that was once the core of the star, which is about the size of the earth, is now called a white dwarf.
For stars with a mass of approximately $M > 5M_\odot$, carbon is able to fuse into even heavier elements like neon and magnesium. The stellar remnants they leave behind are still supported by electron degeneracy pressure and are therefore also called white dwarfs.

2.1.2 Evolution of massive stars

Stars with a mass of approximately $M > 7M_{\odot}$ are able to form heavier elements still, all the way up to iron and nickel, which cannot be fused into heavier elements without losing energy. When the iron core reaches a mass of $1.4M_{\odot}$, known as the Chandrasekhar limit, electron degeneracy pressure is unable to sustain it. The core rapidly collapses under its own gravitation and protons and electrons combine to form neutrons and electron neutrinos. Provided the core is not too massive ($M < 18M_{\odot}$) the collapse is halted by neutron degeneracy pressure. Similar to electron degeneracy pressure, neutron degeneracy pressure prevents neutrons from getting closer together, again due to the Pauli exclusion principle. The neutrinos escaping the core carry away enough energy to eject the outer layers of the star, producing an explosion that is called a supernova.

2.1.3 Pulsars

What remains at the center of a supernova is a small (roughly ∼20 km in diameter), very dense core, mainly consisting of tightly packed neutrons and therefore called a neutron star. During the collapse of the iron core, angular momentum remains conserved and so newly formed neutron stars can spin very rapidly. Rotation periods of young neutron stars can be as short as a tenth of a second. The magnetic flux threading through the core is conserved during the collapse as well, leaving the neutron star with a very strong magnetic field. The fast rotation combined with a strong magnetic field generate a strong electric field. If this electric field is strong enough, it will rip electrons from the neutron star's atmosphere and accelerate them along the magnetic field lines, producing synchroton radiation. This synchroton radiation tends to be aligned along the axes of the magnetic field, creating two beams that point in opposite direction. Neutrons stars that are able to produce these radiation beams are called pulsars (see Fig. 2.1) [7].

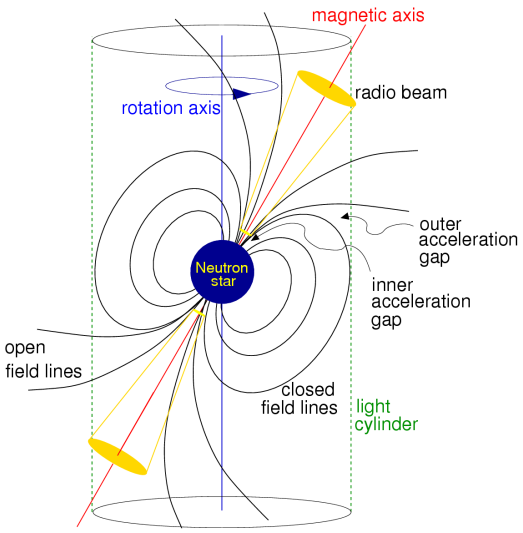

Figure 2.1: A model of a pulsar. Two beams of radiation are aligned along the axis of the magnetic field. The light cylinder represents the distance at which particles co-rotating with the pulsar will be traveling at the speed of light [8].

2.2 Pulsar classes

Pulsars are generally divided in three categories. These are rotation-powered pulsars, accretion-powered pulsars and magnetars. The categories are based on the dominant source of power of the pulsar's radiation.

2.2.1 Rotation-powered pulsars

The radiated energy from rotation-powered pulsars is provided by the loss the of rotational energy as the pulsar's spin frequency decreases. Its energy is constrained by the spin-down luminosity,

$$\dot{E} = -\frac{4\pi^2 I \dot{P}}{P^3} \tag{2.1}$$

which is defined as the maximum amount of energy per second available due to the loss of rotational energy. In this equation, I is the moment of inertia of the spinning pulsar, P the period and $\dot{P}$ the period derivative (see [8] for a derivation).

2.2.2 Accretion-powered pulsars

The radiated energy from accretion-powered pulsars is provided by the gravitational potential energy of accreted matter from a companion star. Accretion-powered pulsars can thus emerge from the binary system of a star and a neutron star. They also tend to have very short rotation periods as they gain the angular momentum from their accreted matter.

2.2.3 Magnetars

The radiated energy from magnetars is thought to be provided by the decay of the magnetic field stored in the interior of the magnetar [9]. The radiated energy from magnetars is substantially higher than their spin-down luminosity and so excludes it from being the magnetar's main source of power. Magnetars have magnetic fields of the order 10^{14}-10^{15} Gauss which is about 10^3 times stronger than other pulsars. They also tend to have relatively long periods of around 2-12 seconds and high period derivatives of the order 10^{-9}-10^{-13} $(s \cdot s^{-1})$. With estimates of a period and period derivative a characteristic age can be calculated with the following equation,

$$\tau = \frac{P}{2\dot{P}} \tag{2.2}$$

with τ the characteristic age, P the period and $\dot{P}$ the period derivative (see [8] for a derivation). The characteristic age for magnetars is then of the order of 10^3-10^6 years. Magnetars are thought to have more complex magnetic fields than shown in Fig. 2.1 due to twisted magnetic field lines.

2.3 Glitches

Usually the rotational parameters of a pulsar are relatively stable, but sometimes they abruptly change significantly in a very short time period. This phenomenon is called a

glitch. The origin of these glitches is not well understood. A common theory is that they are caused by 'starquakes' in the crust of the neutron star. It is thought that these are the result of angular momentum transfer between the neutron star crust and the superfluid below it [10].

2.4 The $(P, \dot{P})$-diagram

The $[P, \dot{P}]$-diagram is a useful diagram for showing the 'demography' of pulsars. It plays a similar role as the Hertzsprung-Russell diagram for the population of stars. It plots the period of the population of pulsars against their period derivative. Several properties of pulsars are correlated with the period and period derivative and they are also displayed in the diagram as contour lines.

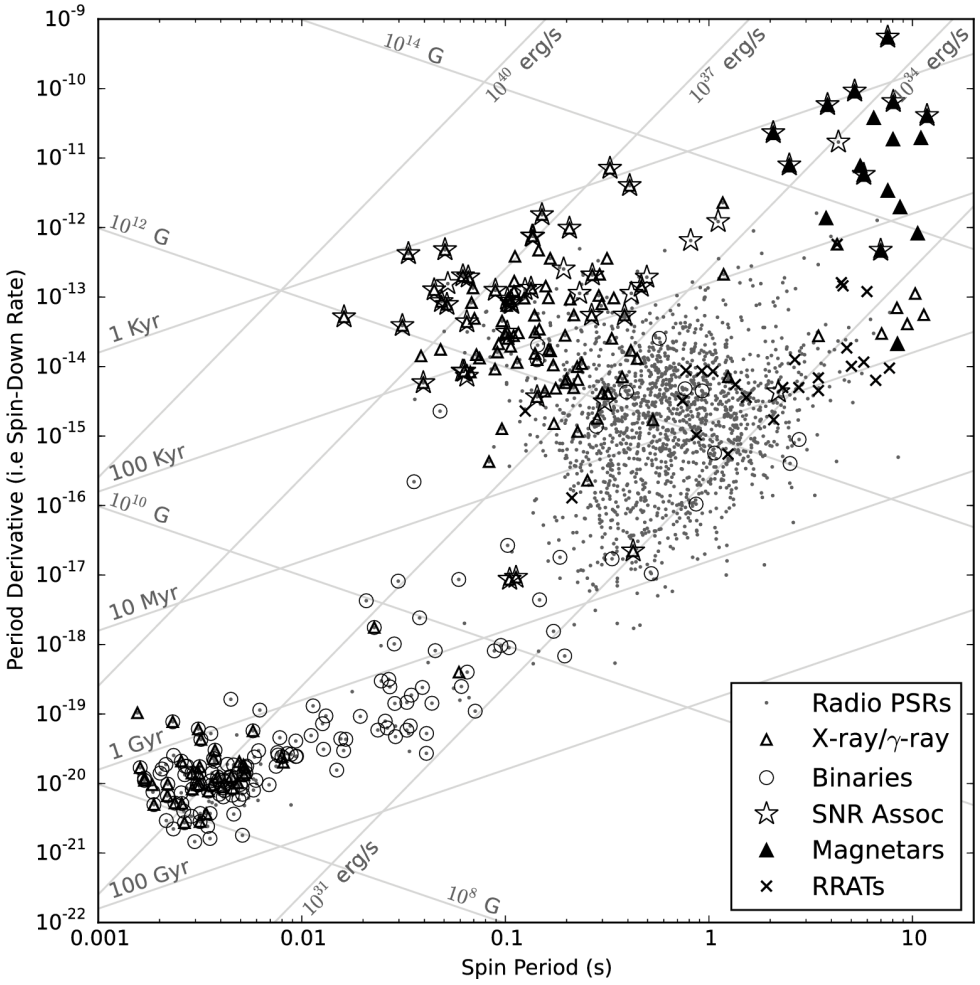

Figure 2.2: A $[P, \dot{P}]$-diagram of a population of pulsars. SNR Assoc indicates pulsars that are associated with supernova remnants and RRAT indicates rotating radio transient, which sporadically emit single pulses instead of continuous pulse trains. The three properties displayed by the contour lines are the spin-down luminosity in erg/s, the magnetic field strength in Gauss and the characteristic age in years. Notice the location of the magnetars as dark triangles, corresponding with a large period, a large period derivative and a strong magnetic field [8].

2.5 4U 0142+61

In this thesis I focus on a particular magnetar, 4U 0142+61. 4U 0142+61 was discovered in 1978 by the Uhuru X-ray observatory [2]. It is located at celestial coordinates $(\alpha, \delta) = (26.5933624, 61.7508861)$ in the constellation Cassiopeia at a distance of about 5.0 kpc [4]. The period and period derivative have been measured at $P = 8.7$ s and $\dot{P} = 2.0 \times 10^{-12}$ s $\cdot$ s^{-1} in 2002 [11]. From these values, the magnetic field strength is estimated to be $1.3 \cdot 10^{14}$ Gauss and the characteristic age ∼70,000 years.
The broad band total high-energy spectrum of 4U 0142+61 was first reported by den Hartog et al. in 2006 [12], including upper-limits derived from CGRO COMPTEL observations covering the MeV-band (0.75-30 MeV). A more detailed description of both the total and pulsed emission spectrum of 4U 0142+61 was given in Kuiper et al. (2006) [13]. An update on the latter work on 4U 0142+61 was presented by den Hartog et al. (2008) [3] in which multi-year observations with INTEGRAL, RXTE, XMM-Newton and ASCA had been used. Figure 2.3 (left) shows the pulse-phase distribution of INTEGRAL ISGRI data for the 20-160 keV band as derived in [3]. The significance of the pulsed emission is 6.5σ using a Z_2^2-test (see Sect. 4.3). Den Hartog et al. (2008) used INTEGRAL ISGRI data collected between Dec. 12, 2003 and Feb. 11, 2007 (i.e. INTEGRAL revolutions 142-528, see Sect. 3.3), representing an effective exposure time of ∼2.8 Ms. The launch of the Fermi gamma-ray space telescope in June 2008 made studies of the high-energy (>30 MeV) gamma-ray properties of 4U 0142+61 possible. In 2010 the first results were published focused on searching for gamma-rays from 4U 0142+61 in the 0.1-10 GeV band using Fermi-LAT data collected across 1.4 years [4] and 1.8 years [5]. No significant emission was detected from 4U 0142+61 both in the spatial and timing domain (see Fig. 2.3 right). Li et al. (2017) reported on searches for gamma-ray emission using 6 years Fermi-LAT data, however, also in this work no significant gamma-ray emission had been detected.

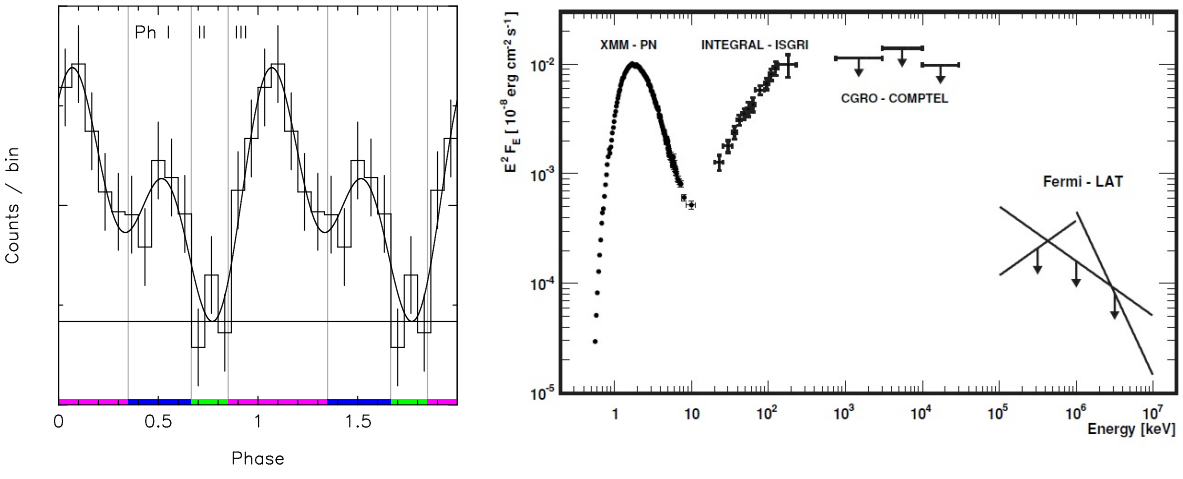

Figure 2.3: Left: Pulse-phase distribution of 4U 0142+61 for the 20-160 keV energy band, derived from INTEGRAL ISGRI data yielding a significance of 6.5σ. The ISGRI data comprises 2.4 Ms of effective exposure time from observations between December 2003 and August 2006 [3]. Right: Wide band total emission spectrum of 4U 0142+61 from soft X-rays up to high-energy gamma-rays. The results of several works were combined in 2010 by Abdo et al. to create this plot [4].

Chapter 3

Instruments

The data used for this research were collected through observations by several space telescopes. This chapter aims to describe the most important characteristics of these space telescopes.

3.1 The Neil Gehrels Swift Observatory

Swift was launched on Nov. 20, 2004 and is still operational today. Swift's main instruments are the Burst Alert Telescope (BAT), the X-Ray Telescope (XRT) and the Ultraviolet/Optical Telescope (UVOT). The BAT is a coded-mask gamma-ray detector with a large field of view. It is sensitive to energies of 15-150 keV and its main purpose is to detect gamma-ray bursts (GRB's) which, if detected, trigger the spacecraft to autonomously point itself in the direction of the bursts. The targets can then be observed with the other instruments for additional and more accurate measurements. The XRT is an X-ray telescope that has a much smaller field of view, but is able to localize targets to approximately 3-5 arcseconds. It is sensitive to energies of 0.2-10 keV. The UVOT is an UV/Optical telescope with a sensitivity to photon wavelengths of 160-600 nm [14].
For the purposes of this research, I only made use of data from the XRT. The XRT has an operation called 'Windowed Timing Mode'. This operation has a high timing resolution of 1.7675 ms which is amply sufficient to characterize the pulse shape of 4U 0142+61.

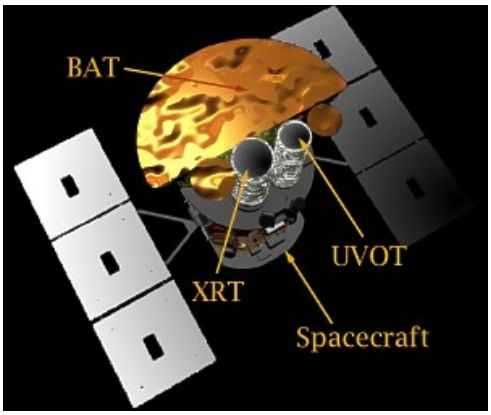

Figure 3.1: The Swift Telescope with its instruments highlighted [15]. The XRT instrument was used in this research to create a timing model of 4U 0142+61.

3.2 NuSTAR

The Nuclear Spectroscopic Telescope Array was launched on June 13, 2012 and is still operational today. NuSTAR is the first focusing high-energy X-ray space telescope, meaning it uses mirrors to direct the hard X-ray photons onto a focal plane.
High-energy photons can only be reflected at small incident angles and so NuSTAR carries a deployable mast to reach the long focal length of 10.14 m. The advantage of this technique is a great increase in sensitivity due to a low amount of background radiation. NuSTAR operates in the hard X-ray band from 3-79 keV. It makes use of two co-aligned Wolter I X-ray telescopes whose focal plane images can be combined to gain sensitivity. The field of view ranges from 6′ to 10′ depending on the photon energy and the absolute temporal resolution is 2-3 ms [16][17][18].

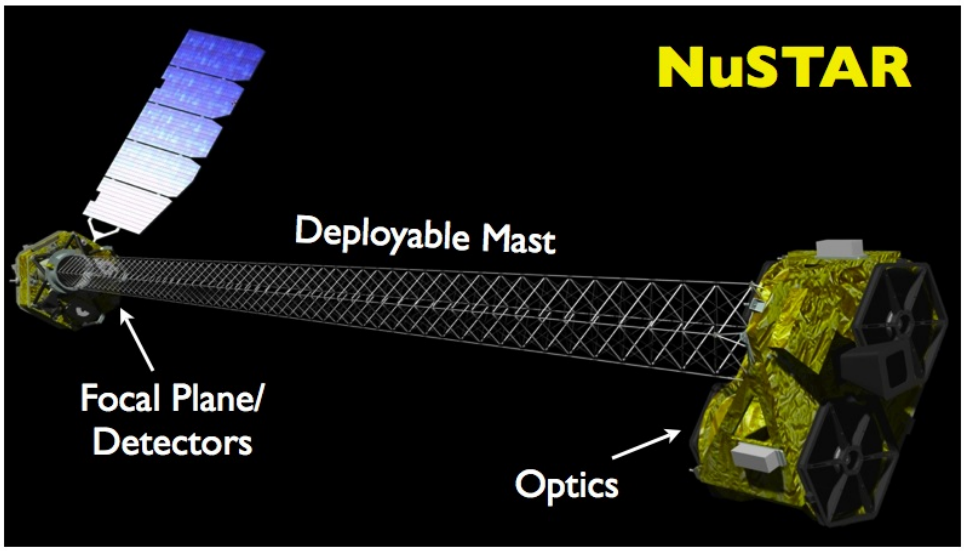

Figure 3.2: NuSTAR with extended mast. The optics contain grazing mirrors that are able to sufficiently bend X-rays between 3 and 79 keV, so that they focus on the focal plane.

3.3 INTEGRAL ISGRI

The International Gamma-Ray Astrophysics Laboratory (INTEGRAL) was launched on Oct. 17, 2002 and is still operational today. It has several instruments on board: a gamma-ray spectrometer SPI, a gamma-ray imager IBIS, an X-ray monitor JEM-X and an optical monitor OMC. As diffraction is negligible at gamma-ray energies, IBIS makes use of a tungsten coded-mask to reconstruct imaging information. IBIS has two detector planes: ISGRI and PICsIT. ISGRI is sensitive between 15 and 1000 keV and PICsIT is sensitive between 100 keV and 10 MeV. For this research, I have used data from the ISGRI instrument. The detector area of ISGRI consists of 8 modules of 64×32 CdTe pixels. Its fully coded field of view is 8.3° by 8.0° and it has an absolute timing accuracy of up to 90 μs [19][20][21]. INTEGRAL observations are organized according to their revolution and subsequently in science windows (scw). One revolution corresponds to the completion of one orbit around the Earth. From launch until early 2015, this took INTEGRAL about 72 hours. In January 2015 the orbit was adjusted and now the duration of one orbit is 64 hours. The counting of revolutions started shortly after launch in October 2002 and the current (June 18, 2019) revolution is 2103. Science windows correspond to stable pointings and are organized in patterns. The pointings of subsequent science windows follow either a 5×5 rectangular dither pattern or a hexagonal pattern, with the source located at the center in both cases [22].

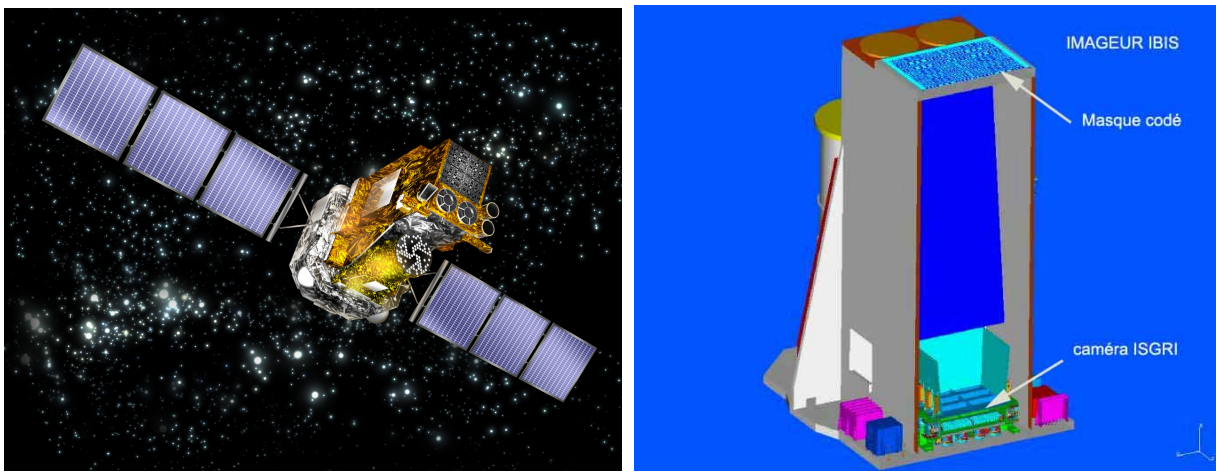

Figure 3.3: Left: the INTEGRAL satellite [20]. Right: the IBIS imager of INTEGRAL. The coded mask casts a shadow on the detectors and from this shadow an image is reconstructed. The distance between the coded mask and the ISGRI detector is 3.2 m [23].

3.4 Fermi Large Area Telescope and Gamma-ray Burst Monitor

The Fermi Gamma-ray Space Telescope (Fermi) was launched on June 11, 2008 and is still operational today. Its two main instruments are the Gamma-ray Burst Monitor (GBM) and the Large Area Telescope (LAT). The GBM instrument consists of twelve sodium iodide scintillators and two bismuth germanate scintillators that, when working together, can cover the full sky. They can detect hard X-rays and gamma-rays between 8 keV and 40 MeV. Its primary objective is to extend the energy range over which gamma-ray bursts can be detected, as the GBM also covers the hard X-ray part of the spectrum. The GBM is also used to locate bursts which the LAT can then autonomously repoint to. [24]. The LAT is a pair-conversion telescope, which means that incoming gamma-rays are converted to an electron-positron pair. By measuring the paths and energies of the pair, the angle at which the photon entered the instrument can be reconstructed. The LAT is sensitive between 20 MeV and 300 GeV and has a wide field of view of 2.4 sr. It has a timing accuracy of less than 10 μs [25].

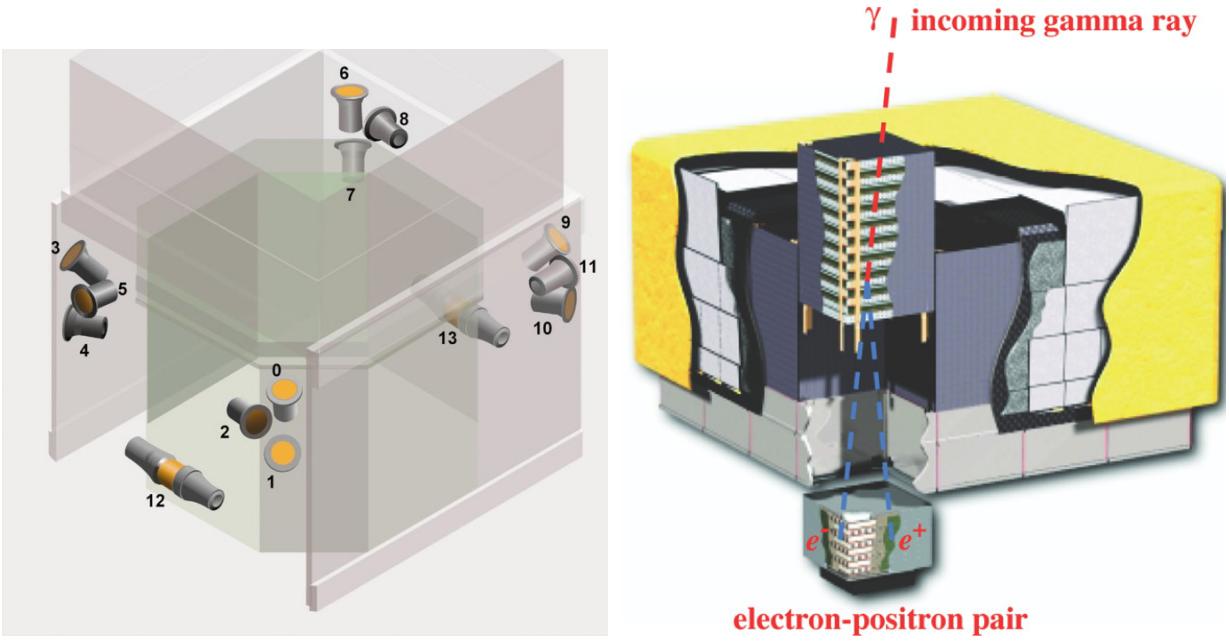

Figure 3.4: Left: the Fermi GBM instrument [24]. Right: the Fermi-LAT instrument. Incoming gamma-rays produce a electron-positron pair which are traced by the instrument to calculate the angle of the incoming gamma-ray [25].

Chapter 4

Data reduction and analysis methods

4.1 Data reduction

The data from the space telescopes were obtained via several online resources. Swift and NuSTAR data were gathered from the High Energy Astrophysics Science Archive Research Center (HEASARC) [26]. INTEGRAL data were gathered from the INTEGRAL Science Data Center (ISDC) [27]. Fermi data were gathered from the Fermi Science Support Center (FSSC) [28]. In the following sections, the criteria for the selection of events will be discussed. Not all events are suitable for analysis for a variety of reasons. The telescopes I have utilized for this research have different instruments, different methods of detection and were used for different parts of the spectrum so the criteria for event selection will vary among telescopes.

4.1.1 Van Allen belts

The space telescopes we have used pass through the van Allen belts. The van Allen belts are a set of regions surrounding the Earth that contain energetic charged particles. These particles trigger the telescopes' instruments and their abundance causes any other astrophysical signals to be indistinguishable. Therefore instruments are turned off during passage through the belts. Most of the telescopes we have used revolve around the Earth in a Low Earth Orbit (LEO) (∼500 km) and only go through a specific part of the van Allen belts called the South Atlantic Anomaly. This is the case for Swift, NuSTAR and Fermi. The boundaries of this region are well defined and the instruments are turned off and on at the well defined times. INTEGRAL, however, does not orbit the Earth in a LEO. The boundaries of the outer belts through which INTEGRAL passes are not precisely known and occasionally the instruments switch off too late or switch on too early, contaminating the first or final parts of an observation. The data from observations need to be screened for anomalies due to passage through the van Allen belts before they can be used. The observations from INTEGRAL between revolution 957 and 2047 (55423-58502 Modified Julian Date (MJD), Aug. 15, 2010 – Jan. 21, 2019) containing 4U 0142+61 were screened visually for this research to check for passage through the van Allen belts and any other anomalies.

4.1.2 Swift-XRT

The Swift-XRT instrument was mainly used for the purpose of making an ephemeris of 4U 0142+61 for the period between July 29, 2011 and Feb. 26, 2015 (55771-57080 in MJD). An ephemeris is a set of parameters of a celestial object during a certain time interval. For 4U 0142+61 in particular, the parameters of interest are its rotation period and the first and second derivative of the rotation period. The final date of the ephemeris is set just before a glitch, where the rotation parameters change dramatically.

The XRT instrument on board of Swift has a few operating modes, one of which is the Windowed Timing Mode. This mode was used for making the ephemeris. The Windowed-Timing mode sacrifices positional information for a high-timing resolution (2.2 ms). Swift observations were rerun through the `xrtpipeline` script with correct source coordinates $(\alpha_{2000}, \delta_{2000}) = (26.5933624, 61.7508861)$. An extraction radius of 25 arcseconds was used and the maximum grade was set to 5. The energy range for selected events was set between 0.50 keV and 10.23 keV.

4.1.3 NuSTAR

The results from the NuSTAR telescope were used to verify the ephemeris made from the Swift data. This is done by comparing the pulse-phase distributions and checking if they are not phase shifted compared to each other. NuSTAR made two long observations of 4U 0142+61 during 27–29 March, 2014, which coincides within the time interval for which I prepared an ephemeris. These have observation identifiers 30001023002 (24 ks) and 30001023003 (144 ks).
The NuSTAR observations were screened according to default criteria in `nupipeline`. An extraction radius of 90″ was used, while the maximum grade was set to 5 and the energy range was set between 3 keV and 80 keV [16][18].

4.1.4 INTEGRAL ISGRI

The data from INTEGRAL were used to create a pulse-phase distribution for energies between 20 and 300 keV. As mentioned in Sect. 3.3, INTEGRAL observations are organized according to their revolution. For this research, data between revolutions 957-2047 (55423-58504 MJD, Aug. 15, 2010 – Jan. 21, 2019) were processed (see table 4.1). INTEGRAL observations of 4U 0142+61 during revolutions 1835-1838 (57938-57948 MJD, July 4, 2017 – July 14, 2017) were not included in the data due to the occurrence of a glitch (timing anomaly, see Sect. 2.3).
Only data that met the following requirements were used: a) the angular separation between the pointing axis and the source during a science window was smaller then to 14.5°, b) I only used events with energies between 15 and 300 keV, c) the minimum and maximum Pixel Illumination Factor (PIF) were set to 0.25 and 1 respectively, meaning that only pixels that were illuminated higher than 25% were taken into account, d) the minimum and maximum ISGRI rise times were 7 and 90 respectively. Noisy pixels were discarded.

Table 4.1: INTEGRAL observations that were processed in this thesis. The last row gives the total. Revs. indicates revolutions, # Scw the number of science windows, GTI exposure the Good-Time-Interval exposure and Eff. exposure is the effective exposure.

Revs.	Date begin	Date end	MJD	GTI exposure (Ms)	Eff. exposure (Ms)	# Scw
957-1071	15-08-2010	24-07-2011	55423-55765	1.656	0.965	596
1073-1490	30-07-2011	27-12-2014	55772-57017	1.487	0.674	604
1565-1977	17-07-2015	18-07-2018	57220-58318	2.865	0.974	854
2038-2047	28-12-2018	21-01-2019	58480-58504	0.801	0.316	226
957-2047	15-08-2010	21-01-2019	55423-58504	6.809	2.929	2280

4.1.5 Fermi-LAT

The Fermi telescope was used to probe the energy range >30 MeV. Similar to data from INTEGRAL, observations where the angular deviation between the source and the pointing of satellite were greater than 15° were discarded. Because the Earth is a source of gamma-rays, events where 4U 0142+61 is blocked by the Earth or where the Earth is significantly in the field of view were discarded. To achieve this, only events with an Earth Zenith angle (angle between the Zenith of the Earth going through the satellite and the pointing of the instrument) of less than 105° were used. The Fermi tool `gtbary`, together with the Solar system ephemeris DE-200, was used to barycenter the events. In June 2015 the Fermi Science Support Center (where our Fermi data were gathered from) adapted a new version of LAT data called Pass 8. This new version improved the effective area of the LAT instrument, which resulted in a better signal-to-background ratio. As is recommended for Pass 8 data I selected only the events with *evclass* = 128 and *evtype* = 3 [29][30].

4.2 Timing Analysis

In order to study the temporal characteristics of 4U 0142+61 we first need accurate measures of 4U 0142+61's period and its derivatives. To achieve this, I barycentered all our data and then I constructed a list of times of arrival (ToA's) to calculate the best fit for an ephemeris. Valid ephemerides are required to construct pulse-phase distributions that show the shape of the pulse at particular energy bands.

4.2.1 Barycentering

In timing studies requiring high accuracy, the times of arrival at the instrument should be converted to arrival times at the 'best' conceivable inertial frame. The most suitable inertial frame for our purposes is the center of mass, also called barycenter, of the Solar System. The conversion of an arrival time at the instrument to the arrival time at an inertial reference frame is called barycentering. Several corrections need to be taken into account [8].

- Travel time differences between Earth and the Solar System barycenter as viewed from 4U 0142+61 constitute the largest correction component as the diameter of Earth's orbit is about 10^3 lightseconds. This is called the Römer delay.
- The effect of gravitational redshift and time dilation needs to be taken into account. This is called the Einstein delay.
- The correction for the curvature of spacetime in the Solar System is called the Shapiro delay.

There are other corrections as well, but these are negligible in our case. For the position of the Sun and the planets, I used the Solar System ephemeris DE-200, provided by the Jet Propulsion Laboratory (JPL) [31]. For the position of the 4U 0142+61, I used the celestial coordinates $(\alpha, \delta) = (26.5933624, 61.7508861)$ [32]. The barycentering process was applied to all data used in this research.

4.2.2 Determination of an ephemeris

The first step in creating an ephemeris is establishing a list of ToA's. ToA's are derived from observations that contain enough data to produce significant ($> 3\sigma$) pulsed signals. With Swift-XRT data, this corresponds to observations with a duration of approximately one hour at minimum. Most observations of 4U 0142+61 by Swift-XRT have a duration of about one hour, however, shorter observations also exist. Data from consecutive shorter observations, that would not have produced a significant pulse signal on their own, were combined together to create one 'larger' observation, provided that the time between the smaller observations was no more than a few days.
The gravity-point i.e. the middle of an observation is initially taken as the ToA of that observation. However, the set of ToA's that constitute gravity-points of the observations are phase-incoherent, as they are each located at an arbitrary point in the phase. To create a set of phase-coherent ToA's, we first create pulse-phase distributions from the observations. We scan across a frequency interval which should contain the genuine rotation frequency to yield a best estimate of the rotation frequency that will produce the most significant pulse-phase distribution. Then, we cross-correlate the optimal pulse-phase distribution with a high-statistics template distribution. The global maximum in the correlation diagram determines the time shift to be applied to the gravity-point ToA of the pulse-phase distribution to align it with the template (see [33] for a more detailed explanation). Having established a set of phase-coherent ToA's, we can use the following equation to 'fold' the arrival times and calculate the phase residuals at the respective arrival times.

$$\Phi(t) = -\Phi_0 + \nu(t - t_0) + \frac{1}{2}\dot{\nu}(t - t_0)^2 + \frac{1}{6}\ddot{\nu}(t - t_0)^3, \tag{4.1}$$

where t is a ToA, $\Phi(t)$ the predicted phase at that ToA, Φ_0 is the phase at the reference point in time t_0 (also known as the epoch of the ephemeris), ν the rotational frequency and $\dot{\nu}$ and $\ddot{\nu}$ its first and second derivative respectively. By taking the fractional part of $\Phi(t)$ we obtain the phase residual. We then calculate the ν, $\dot{\nu}$ and $\ddot{\nu}$ for which the phase residuals best fitted a horizontal line. I used this procedure to construct an ephemeris for the period between July 29, 2011 and Feb. 26, 2015 (see entry nr. 3 in Table 5.1). The phase residuals of ToA's derived from Swift-XRT data that were produced by the best ephemeris for this period are shown in Fig. 5.1.

4.2.3 Pulse-phase distributions

Having acquired valid ephemerides, we can construct pulse-phase distributions. Pulse-phase distributions are displayed as histograms with each bin containing the number of events sampled during a particular interval in phase. Events can be sorted on their energy so that pulse-phase distributions show the pulse shape for a particular energy range. Because 4U 0142+61 is not particularly luminous, the observation of individual pulses across a phase cycle does not contain sufficient events from the source to distinguish the shape of the pulse from the background radiation. However, by adding the counts of equivalent bins from different cycli together, the shape of a 'pulse' may eventually appear. Given a steady pulsed emission of photons from the source, the 'stacking' of more and more phases from different cycli should increase the significance of the pulsed emission (see Fig. 4.1).

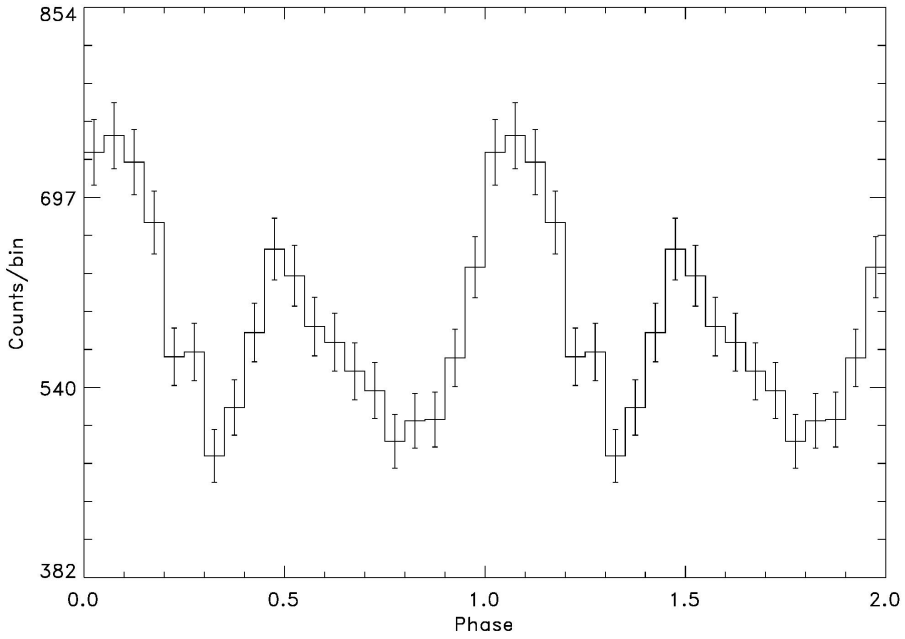

Figure 4.1: Example of a pulse-phase distribution. The events contained in these bins have three main sources. Most of the events are due to background radiation, but this constitutes a statistically flat distribution. A small part consists of unpulsed radiation from the source, but this component is also 'flat'. Finally, the pulsed events from the source form the underlying pulse pattern. For visual purposes two identical cycli are shown.

4.3 Statistics

For the assessment of the significance of pulse-phase distributions I used the Z_n^2 statistic [34], which is based on a Fourier analysis on event basis:

$$Z_n^2 = \frac{2}{N}\sum_{k=1}^{n}[(\sum_{i=1}^{N} cosk\phi_i)^2 + (\sum_{i=1}^{N} sink\phi_i)^2], \tag{4.2}$$

where ϕ_i is the phase of an event, N the total number of events and n the number of harmonics. The Z_n^2 distribution follows the χ^2 distribution with $2n$ degrees of freedom. Unlike the χ^2 distribution though, the Z_n^2 distribution is not sensitive to the number of bins used [35]. It gives a measure of the signal-to-noise ratio and can be used to calculate the significance of the pulsed signal expressed in Gaussian sigma (σ).

Chapter 5

Results

For this research I first derived an ephemeris for the period between July 29, 2011 and Feb. 26, 2015 (55771-57080 in MJD) using data from the Swift-XRT instrument (see Fig. 5.1). I verified this ephemeris and studied the energy dependence of the morphology of the pulse profiles by constructing pulse-phase distributions from Swift-XRT and NuSTAR data (see Fig. 5.2) and comparing the mutual alignment of the phase distributions. The phase distributions from Swift data are fitted adopting 2 harmonics, while phase distributions from NuSTAR data are fitted adopting 4 harmonics. Four harmonics are more appropriate for NuSTAR, because NuSTAR is substantially more sensitive and greater detail in pulse-phase distributions should be expected. Together with ephemerides that were prepared by my supervisor, we now had measures of 4U 0142+61's rotational parameters covering a period of almost 11 years (Aug. 4, 2008 – Jan. 23 2019). The complete list of ephemerides used for this period is shown in Table 5.1. The INTEGRAL ISGRI data derived from observations between Aug. 15, 2010 and Jan. 21, 2019 (see Table 4.1) were used to construct pulse-phase distributions for energies between 20 and 300 keV (see Fig. 5.3). The INTEGRAL data from this period could also be combined with the INTEGRAL data between 2003 and 2008 that had already been processed at SRON [3]. With this data, collected over a 16-year period, a considerable increase in significance has been made with respect to the first publication by den Hartog et al. [3] (see Fig. 5.4). I also used the ephemerides in Table 5.1 to create pulse-phase distributions for Fermi-LAT data between Aug. 4, 2008 and Jan. 21, 2019, but significant pulsed high-energy gamma-ray radiation was not discovered (see Fig. 5.5).

Table 5.1: Ephemerides of 4U 0142+61 that were utilized for creating pulse-phase distributions. The ephemeris with entry nr. 3 was produced in this work and covers a period of approximately 3.6 years.

Entry	Start [MJD]	End [MJD]	t_0, Epoch [MJD]	ν [Hz]	$\dot{\nu}$ $\times 10^{-14}$ [Hz/s]	$\ddot{\nu}$ $\times 10^{-23}$ [Hz/s^2]	Φ_0
1	54682	55315	54713	0.1150900037859	-2.74516	3.6000	0.751
2	55203	55763	55329	0.1150885887349	-2.60829	0.0000	0.526
3	55771	57080	56512	0.1150864179544	-2.62309	0.0704	0.042
4	57175	57937	57762	0.1150835483576	-2.62747	0.0000	0.716
5	57949	58064	57949	0.1150833807600	-4.17577	-221.00	0.271
6	58063	58506	58237	0.1150824572718	-2.69219	4.6400	0.683

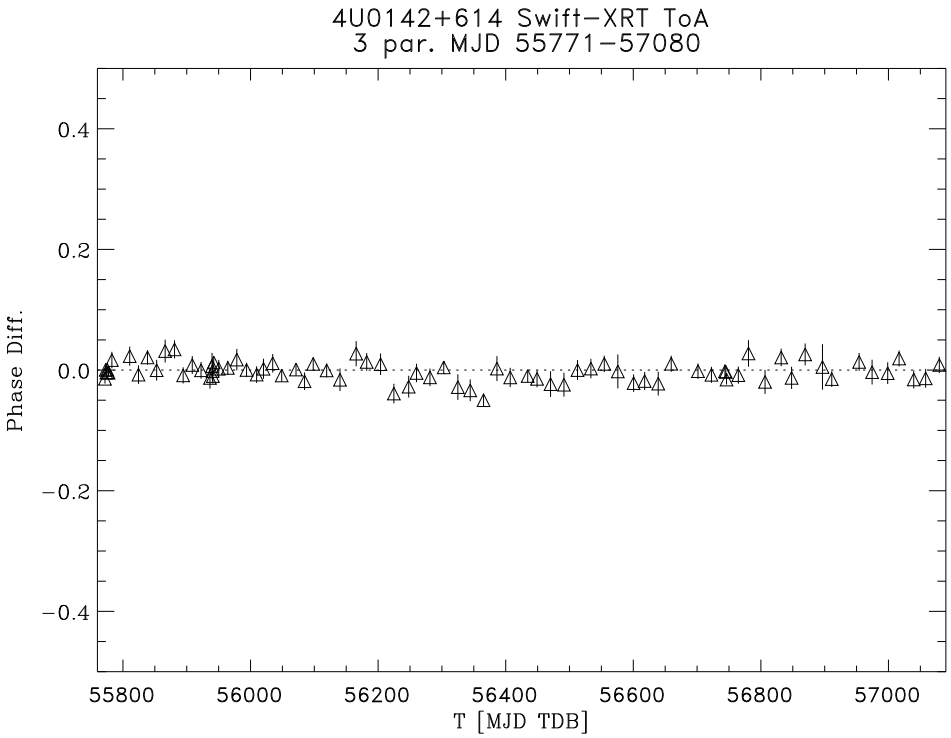

Figure 5.1: Phase residuals of ToA's derived from Swift-XRT data. Phase residuals were determined with Eq. 4.1 and the ephemeris with entry nr. 3 in Table 5.1 with MJD 55771-57080 (July 29, 2011 – Feb. 26, 2015).

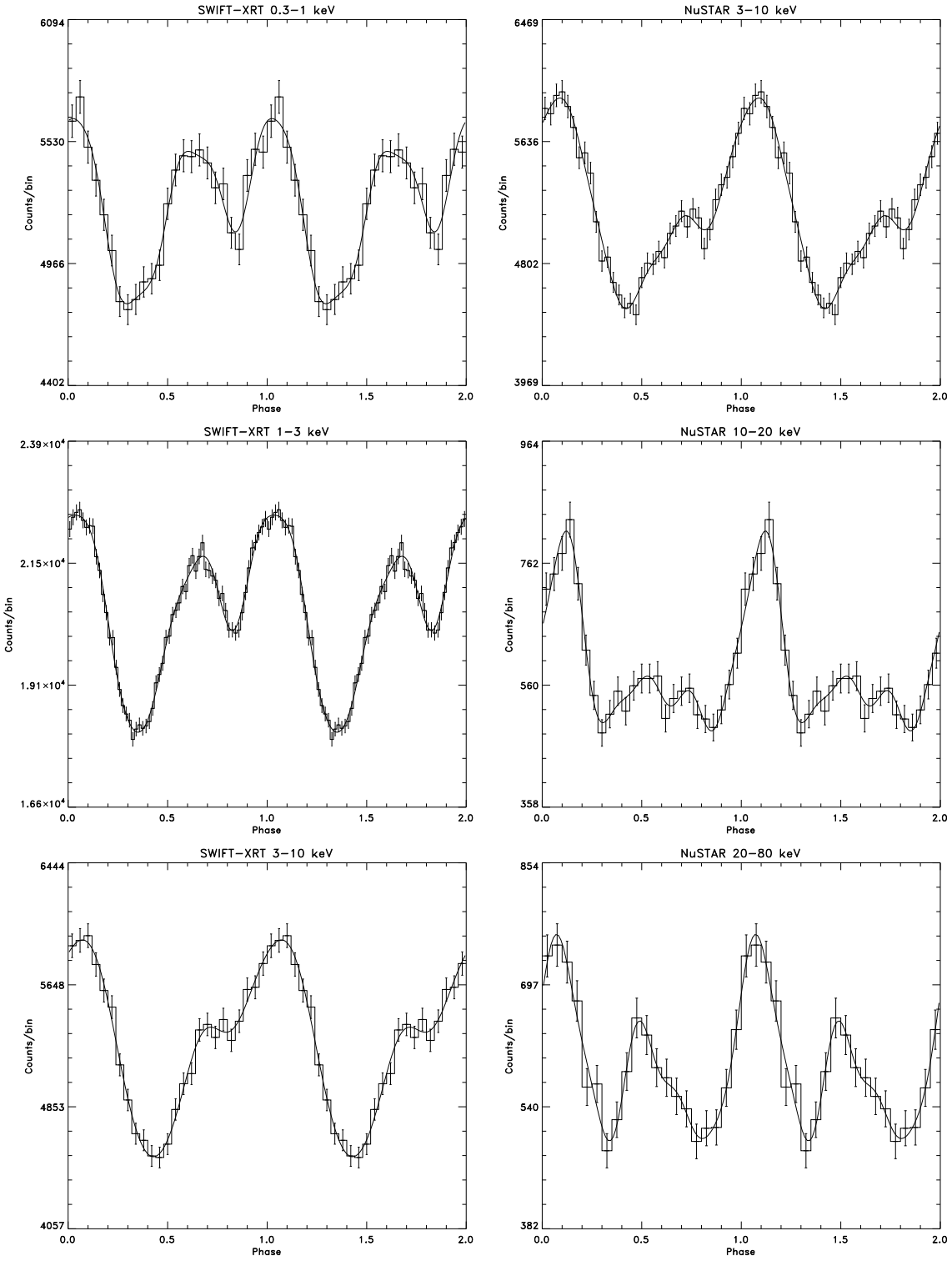

Figure 5.2: Pulse-phase distributions (shown twice for clarity) for energy intervals between 0.3 and 80 keV, derived from Swift-XRT and NuSTAR data with superposed Fourier fits. The significances for Swift are 25.4σ, 33.4σ and 32.4σ for energy ranges 0.3-1 keV, 1-3 keV and 3-10 keV, respectively, adopting 2 harmonics. The significances for NuSTAR are 32.5σ, 24.8σ and 18.3σ for energy ranges 3-10 keV, 10-20 keV and 20-80 keV, respectively, adopting 4 harmonics.

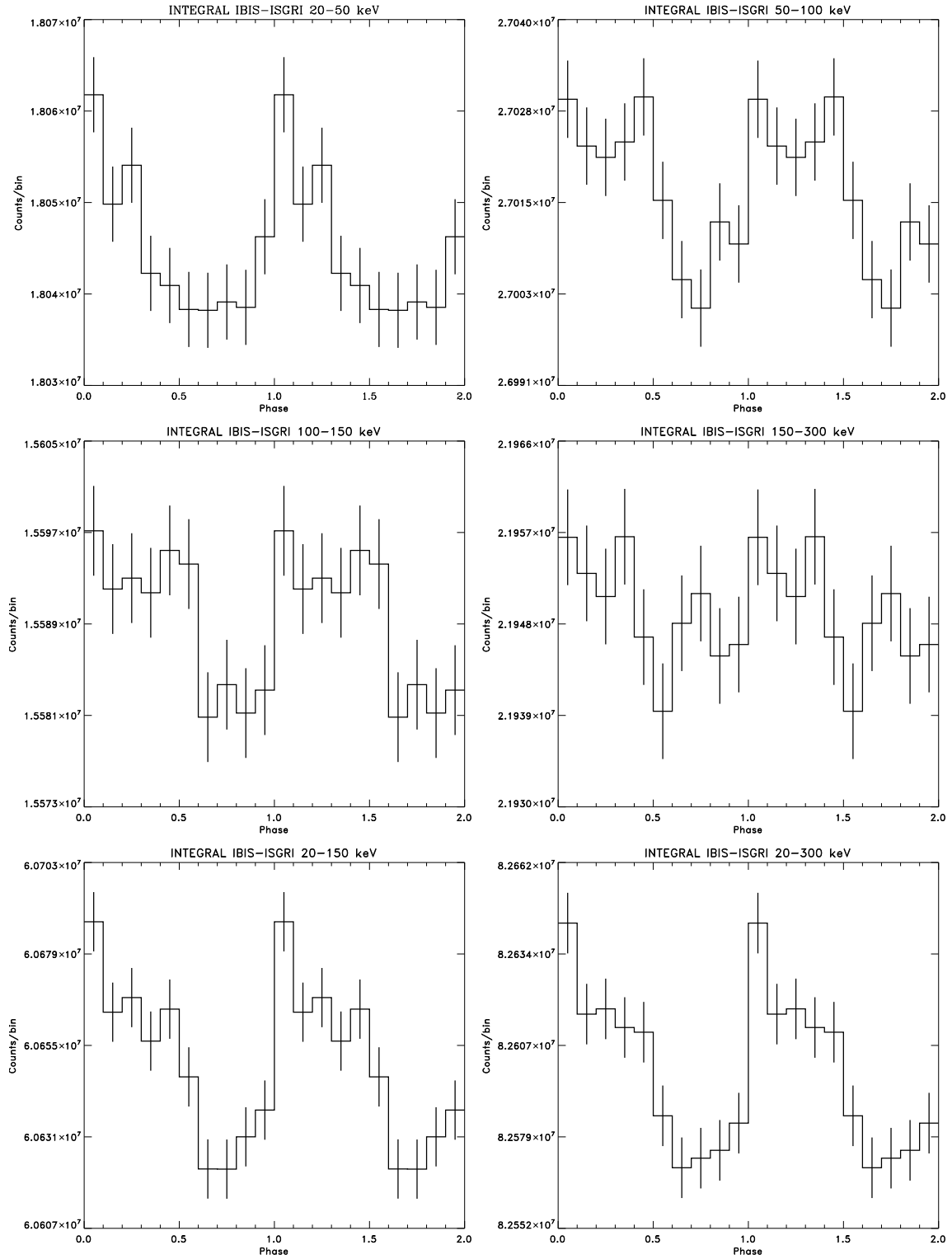

Figure 5.3: Pulse-phase distributions derived from INTEGRAL ISGRI data gathered between revolutions 957 and 2047 (Aug. 15, 2010 – Jan. 21, 2019) for energy intervals between 20 and 300 keV. The data from this period were processed in this work and contains 2.9 Ms of effective exposure time. The significances are 4.2σ, 4.3σ, 3.4σ, 1.3σ, 6.9σ and 6.5σ for energy ranges 20-50 keV, 50-100 keV, 100-150 keV, 150-300 keV, 20-150 keV and 20-300 keV, respectively, considering 2 harmonics.

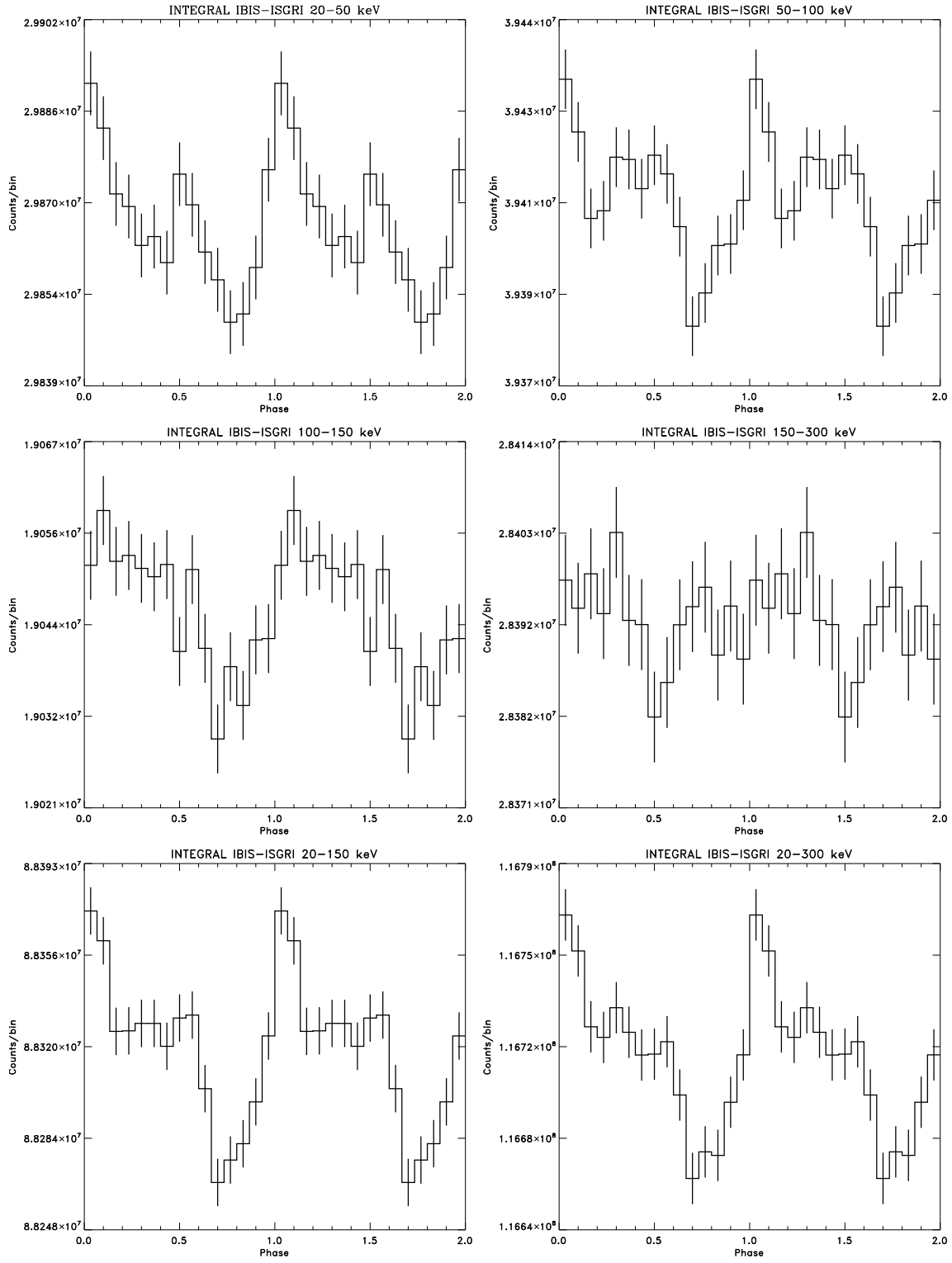

Figure 5.4: Pulse-phase distributions derived from INTEGRAL ISGRI data gathered between revolutions 142 and 2047 (Dec. 12, 2003 – Jan. 21, 2019) for energy intervals between 20 and 300 keV. Here, INTEGRAL data that were processed in this work are combined with INTEGRAL data that had already been processed. These data comprise all available INTEGRAL observations of 4U 0142+61 with the ISGRI instrument that have been made up to 21 Jan 2019. The significances are 6.7σ, 6.2σ, 5.4σ, 1.3σ, 10.7σ and 9.3σ for energy ranges 20-50 keV, 50-100 keV, 100-150 keV, 150-300 keV, 20-150 keV and 20-300 keV, respectively, considering 2 harmonics.

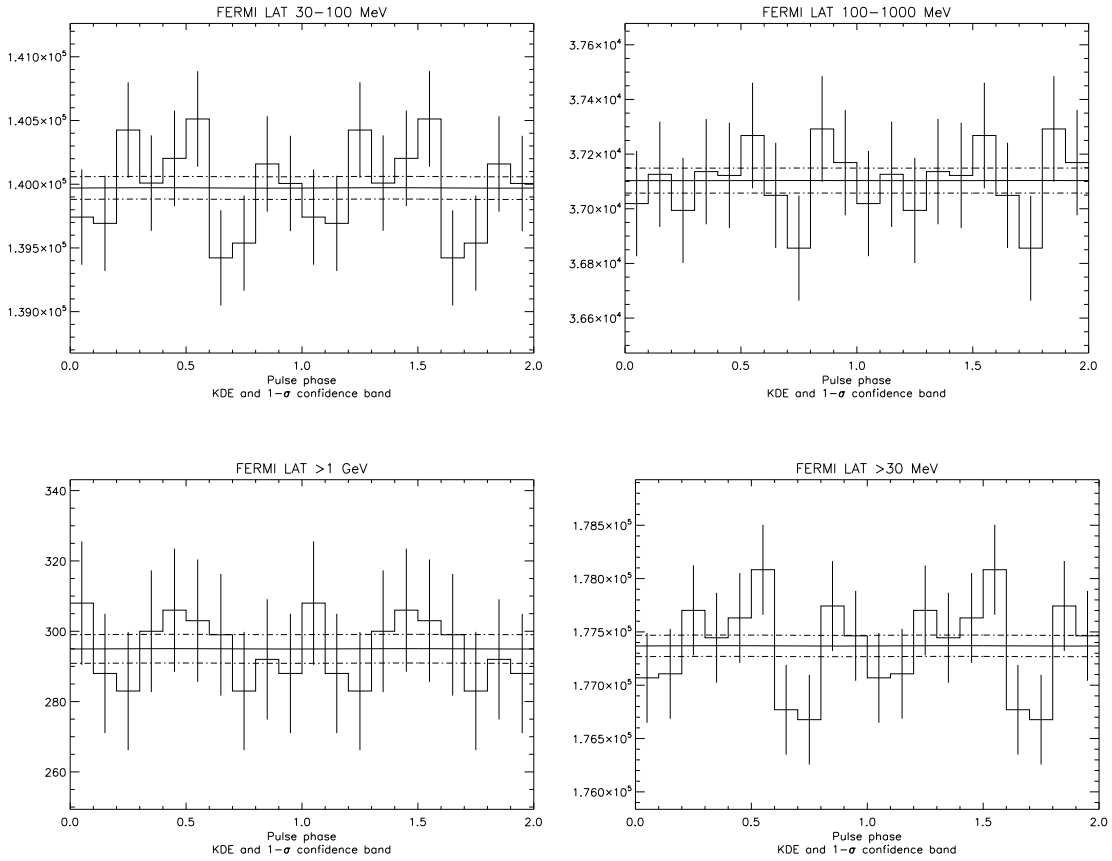

Figure 5.5: Pulse-phase distributions for energy intervals >30 MeV, derived from Fermi-LAT data gathered between Aug. 4, 2008 and Jan. 21, 2019. The significances of the pulse-phase distributions are $< 1\sigma$ for all energy bands, adopting 2 harmonics.

Chapter 6

Discussion and Conclusions

In this bachelor thesis I have investigated magnetar 4U 0142+61's high-energy temporal characteristics by determining pulse-phase distributions for high-energy bands. I have done this by analyzing data from the INTEGRAL ISGRI and Fermi-LAT instruments, which are sensitive to energies between 20-300 keV and >30 MeV, respectively. Unique to this research was the long exposure time of 4U 0142+61 that was covered. The data from INTEGRAL ISGRI observations performed between Aug. 15, 2010 and Jan. 21, 2019, that were processed in this research, added 2.9 Ms of exposure time to the already existing processed data. These data combined encompass all INTEGRAL ISGRI observations made of 4U 0142+61 up until January 2019. With these data, a pulse-phase distribution was constructed with a significance of 10.7σ for energies between 20 and 150 keV. However, in spite of the long exposure, pulsed emission could still not be detected in the 150-300 keV band.
In this work, high-energy gamma-ray data (>30 MeV) from the Fermi-LAT have also been analyzed in a timing study that has been collected across a more than 10 year period: i.e. Aug. 4, 2008 - Jan. 21, 2019. The whole period was covered with valid (and verified) ephemerides (small intervals around timing glitches were excluded). Unfortunately, the pulsed emission significances for energies >30 MeV were all below 1σ adopting 2 harmonics in the Z^2-test. Previous studies using Fermi-LAT data [4][6][5] utilized significantly less exposure than in current work: e.g. in [4] only 1.4 years exposure time, [5] 1.8 years, while in [6] 6 years has been used in a spatial study but valid contemporaneous timing models were lacking contrary to our work. From our non-detections of pulsed emission at >30 MeV, significantly more constraining flux upper-limits, compared to those reported in [4][6][5], will be derived in forthcoming work. As a doubling of the exposure time (as would be acquired from observations over roughly another 10 year period) would only increase the significance by approximately a factor of $\sqrt{2}$, more exposure time for the >30 MeV energy range would very likely not result in a detection of pulsed emission of 4U 0142+61 at high-energy gamma-rays. Unfortunately, Fermi-GBM (8 keV - 40 MeV) data have not been analyzed in this bachelor project, although initially scheduled, because of time limitations. Of the current active high-energy instruments, only from Fermi GBM data significant progress is expected in the description of the pulsed emission spectrum of 4U 0142+61 at energies between 100-1000 keV i.e. the spectral break energy window. This work is ongoing at SRON and initial results using more than 10 years of Fermi-GBM exposure time show (very) significant ($\sim 8\sigma$) pulsed emission in the 100-300 keV band. Even more intriguing, very likely pulsed emission is now detected for the first time in the 300-540 keV band. This makes an accurate spectral description of the break area

possible, and so provide crucial information for spectral modelling.
Further progress in the characterization of high-energy spatial/spectral and timing properties will have to come from a new generation of space telescope missions, making it possible to probe the spectral break area, 100-1000 keV, in great detail.

Chapter 7

Acknowledgement

I am very grateful that I have been granted the opportunity to do my bachelor thesis at SRON. It has taught me much about doing astronomical research, working in an institute and writing a scientific paper. I would especially like to thank my supervisor Dr. Lucien Kuiper for guiding me throughout this project. His availability for advice and feedback, attention to detail and overall support have been invaluable for this research. I would also like to thank Dr. Tomislav Prokopec for making this project possible by being my contact at Utrecht University.

Bibliography

[1] Lucy Conklin Illustration: Magnetar. URL `https://www.lucyconklin.com/pages/magnetar.html`.

[2] W. Forman et al. The fourth Uhuru catalog of X-ray sources. *The Astrophysical Journal*, (38:357-412), 1978.

[3] P. den Hartog et al. Detailed high-energy characteristics of AXP 4U0142+61. Multi-year observations with INTEGRAL, RXTE, XMM-Newton, and ASCA. *Astronomy and Astrophysics*, (489:245-261), 2008.

[4] A.A. Abdo et al. Search for gamma-ray emission from magnetars with the Fermi Large Area Telescope. *The Astrophysical Journal*, (725:L73-L78), 2010.

[5] S. Şaşmaz Muş and E. Göğüş. Search for high-energy gamma-ray emission from an anomalous X-ray pulsar, 4U 0142+61. *The Astrophysical Journal*, (723:100-103), 2010.

[6] J. Li et al. Gamma-ray upper limits on magnetars with six years of Fermi-LAT observations. *The Astrophysical Journal*, (835:30), 2017.

[7] Barbara Ryden and Bradley M. Peterson. *Foundations of Astrophysics*. Addison-Wesley (Pearson Education), 2011.

[8] James J. Condon and Scott M. Ransom. *Essential Radio Astronomy*. Princeton University Press, 1 edition, 2016.

[9] R.C. Duncan and C. Thompson. Formation of very strongly magnetized neutron stars: implications for gamma-ray bursts. *The Astrophysical Journal*, (392:L9-L13), 1992.

[10] J.M. Lattimer and M. Prakash. The physics of Neutron Stars. *Science*, (304:5670), 2004.

[11] F.P. Gavriil and V.M. Kaspi. Long-term Rossi X-ray Timing Explorer monitoring of anomalous X-ray pulsars. *The Astrophysical Journal*, (567:1067-1076), 2002.

[12] P. den Hartog et al. INTEGRAL survey of the Cassiopeia region in hard X-rays. *Astronomy and Astrophysics*, (451:587-602), 2006.

[13] L. Kuiper et al. Discovery of luminous pulsed hard X-ray emission from anomalous X-ray pulsars 1RXS J1708-4009, 4U 0142+61, and 1E 2259+586 by INTEGRAL and RXTE. *The Astrophysical Journal*, (645:556-575), 2006.

[14] *The Swift Technical Handbook, Version 13.0*. Swift Science Center, 2016.

[15] Mission Operations Center for Swift, PennState University. URL `https://www.swift.psu.edu/`.

[16] F.A. Harrison et al. The Nuclear Spectroscopic Array (NuSTAR) high-energy X-ray mission. *The Astrophysical Journal*, (770:103), 2013.

[17] Goddard space flight center, About NuSTAR. URL `https://heasarc.gsfc.nasa.gov/docs/nustar/nustar_about.html`.

[18] K.K. Madsen et al. Calibration of the NuSTAR High-energy Focusing X-ray Telescope. *The Astrophysical Journal Supplement Series*, (220:8), 2015.

[19] ESA, IBIS: Imager on Board the INTEGRAL Satellite, . URL `https://www.cosmos.esa.int/web/integral/instruments-ibis`.

[20] ESA, About INTEGRAL, . URL `https://www.cosmos.esa.int/web/integral/mission-overview`.

[21] F. Lebrun et al. ISGRI: The INTEGRAL Soft Gamma-Ray Imager. *Astronomy and Astrophysics*, (411:L141-L148), 2003.

[22] *Announcement of Opportunity for Observing Proposals (AO-16)*. INTEGRAL, Science Operations Centre, 2018.

[23] ISGRI: a camera for invisible light(CEA). URL `http://irfu.cea.fr/dap/Phocea/Vie_des_labos/Ast/ast_visu.php?id_ast=1371`.

[24] C. Meegan et al. The Fermi Gamma-ray Burst Monitor. *The Astrophysical Journal*, (702:791-804), 2009.

[25] W.B. Atwood et al. The Large Area Telescope on the Fermi gamma-ray space telescope mission. *The Astrophysical Journal*, (697:1071-1102), 2009.

[26] High Energy Astrophysics Science Archive Research Center (HEASARC), NASA. URL `https://heasarc.gsfc.nasa.gov/docs/cgro/db-perl/W3Browse/w3browse.pl`.

[27] INTEGRAL Science Data Center (ISDC), ESA. URL `https://www.isdc.unige.ch/integral/archive`.

[28] Fermi Science Support Center (FSSC), NASA. URL `https://fermi.gsfc.nasa.gov/ssc/`.

[29] Using LAT's new Pass 8 data, FSSC. URL `https://fermi.gsfc.nasa.gov/ssc/data/analysis/documentation/Pass8_usage.html`.

[30] L. Kuiper et al. The Fermi-LAT detection of magnetar-like pulsar PSR J1846-0258 at high-energy gamma-rays. *Monthly Notices of the Royal Astronomical Society*, (475:1238-1250), 2018.

[31] E.M. Standish Jr. The observational basis for JPL's DE 200, the planetary ephemerides of the Astronomical Almanac. *Astronomy and Astrophysics*, (233:252-271), 1990.

[32] F. Hulleman et al. The Anomalous X-ray Pulsar 4U 0142+61: Variability in the infrared and a spectral break in the optical. *Astronomy and Astrophysics*, (416:1037-1045), 2004.

[33] L. Kuiper et al. High-energy characteristics of the schizophrenic pulsar PSR J1846-0258 in Kes 75. *Astronomy and Astrophysics*, (501:1031-1046), 2009.

[34] R. Buccheri et al. Search for pulsed gamma-ray emission from radio pulsars in the COS-B data. *Astronomy and Astrophysics*, (128,245-251), 1983.

[35] J.M. Fierro. *Observations of spin-powered pulsars with the EGRET gamma-ray telescope*. PhD thesis, Stanford University, 12 1995. pages 52-53.